

# Neuro-Planner: A 3D Visual Navigation Method for MAV with Depth Camera based on Neuromorphic Reinforcement Learning

Junjie Jiang , Delei Kong , Kuanxu Hou , Xinjie Huang , Hao Zhuang  and Zheng Fang , *Member, IEEE*

**Abstract**—Traditional visual navigation methods of micro aerial vehicle (MAV) usually calculate a passable path that satisfies the constraints depending on a prior map. However, these methods have issues such as high demand for computing resources and poor robustness in face of unfamiliar environments. Aiming to solve the above problems, we propose a neuromorphic reinforcement learning method (Neuro-Planner) that combines spiking neural network (SNN) and deep reinforcement learning (DRL) to realize MAV 3D visual navigation with depth camera. Specifically, we design spiking actor network based on two-state LIF (TS-LIF) neurons and its encoding-decoding schemes for efficient inference. Then our improved hybrid deep deterministic policy gradient (HDDPG) and TS-LIF-based spatio-temporal back propagation (STBP) algorithms are used as the training framework for actor-critic network architecture. To verify the effectiveness of the proposed Neuro-Planner, we carry out detailed comparison experiments with various SNN training algorithm (STBP, BPTT and SLAYER) in the software-in-the-loop (SITL) simulation framework. The navigation success rate of our HDDPG-STBP is 4.3% and 5.3% higher than that of the original DDPG in the two evaluation environments. To the best of our knowledge, this is the first work combining neuromorphic computing and deep reinforcement learning for MAV 3D visual navigation task.

**Index Terms**—Visual navigation, depth camera, deep reinforcement learning, actor-critic network, neuromorphic computing.

## I. INTRODUCTION

**A**UTONOMOUS navigation in GPS-denied environment is one of the most core issues in the field of mobile robots, especially for the autonomous navigation of micro aerial vehicle (MAV). Due to the limited load capacity of MAV, only lightweight sensor modules can be carried. Therefore, vision sensors with small size, lightweight, low power consumption and rich information are very suitable for MAV navigation [1] [2]. Visual autonomous navigation of MAV

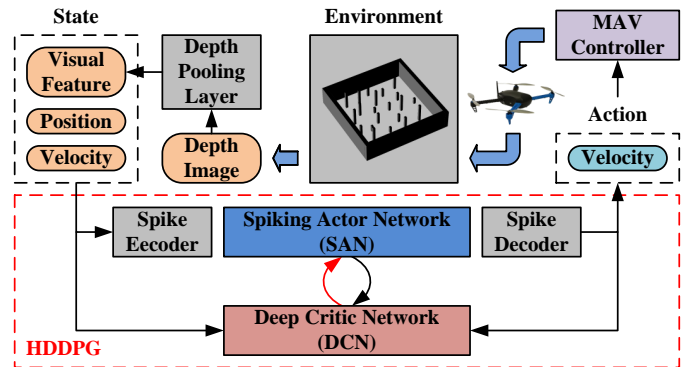


Fig. 1. Overview of the proposed Neuro-Planner architecture. In the training part, the hybrid deep deterministic policy gradient (HDDPG) algorithm is used to train the entire actor-critic network. In the testing part, only spiking actor network is used for inference to realize the MAV autonomous navigation.

means that MAV system can perceive the surrounding environment and independently complete obstacle avoidance and navigation from the starting point to the goal point. At present, the main visual autonomous navigation framework of MAV usually relies on mapping technology. Firstly, a 3D map of the environment are constructed by visual sensors, then the path that can honor traversability constraints is calculated by global and local planners. Finally, the generated paths are tracked by controllers [3] [4] [5] [6] [7] [8] [9]. In essence, this autonomous navigation paradigm calculates the passable path through certain constraints, which is difficult to adapt to the complex and changeable real environments. Therefore, it is still far behind the expected intelligence of humans.

In comparison, the processing mechanism of biological visual navigation system in nature is completely different from that of traditional autonomous navigation system. This is mainly reflected in the following two aspects: First, biological visual navigation system does not need to accurately calculate and model the ontology and the surrounding environment but uses the experience of interaction with environment previously to determine the current action. And it further improves the later action through the feedback of current action. Second, biological visual navigation system processes information hierarchically, parallelly, cyclically and asynchronously in a dynamic neural network composed of hundreds of millions of spiking neurons.

Manuscript created December 23, 2021. This work was supported by National Natural Science Foundation of China (62073066, U20A20197), Intel Neuromorphic Research Community (NRC) Grant Award (RV2.137.Fang), Science and Technology on Near-Surface Detection Laboratory (6142414200208), the Fundamental Research Funds for the Central Universities (N2226001), and Aeronautical Science Foundation of China (No.201941050001). (*Corresponding author: Zheng Fang.*)

Junjie Jiang, Kuanxu Hou, Xinjie Huang and Zheng Fang are with Faculty of Robot Science and Engineering, Northeastern University, Shenyang, China (e-mail: 2001998@stu.neu.edu.cn, 2001995@stu.neu.edu.cn, 2101979@stu.neu.edu.cn, fangzheng@mail.neu.edu.cn).

Delei Kong and Hao Zhuang are with College of Information Science and Engineering, Northeastern University, Shenyang, China (e-mail: kong.delei.neu@gmail.com, 2100922@stu.neu.edu.cn).

These phenomena arises great interest of researchers, and gives birth to two research fields: reinforcement learning (RL) [10] and spiking neural network (SNN) [11]. To gain experience as animals, RL is proposed. RL imitates the behavior paradigm of interaction between biology and environment. It makes agents interact with the environment continuously to gain experience to improve the navigation policy by setting reasonable reward function to realize the independent decision-making ability of agents. Autonomous navigation based on RL shows better success rate and robustness than traditional methods when facing unknown environments. To imitate the biological processing of brains, SNN is proposed. Spiking neurons in SNN execute asynchronously and independently, and thus have greater flexibility as well as the ability to learn temporal information. Compared with artificial neural network (ANN), SNN has advantages of more complex spatio-temporal dynamics, rich spiking coding mechanisms and high energy efficiency.

In this paper, we aim to combine deep reinforcement learning and spiking neural network to solve the visual autonomous navigation problem of MAV facing unknown environments<sup>1</sup>. The main innovations and contributions of this paper are as follows:

- Aiming at the MAV 3D visual navigation task, a spiking actor network (SAN) based on two-state LIF (TS-LIF) spiking neurons and its encoding-decoding schemes (including state normalization, uniform encoding, rate decoding, and setting velocity mapping) are proposed. By processing the encoded state and visual observation, the action is obtained and decoded into control commands sent to low-level MAV controller.
- We propose a hybrid deep deterministic policy gradient (HDDPG) reinforcement learning algorithm based on actor-critic networks (ACN), and improve spatio-temporal back propagation (STBP) for SAN training based on TS-LIF spiking neurons.
- A software in-the-loop (SITL) simulation system of MAV is built based on ROS, Gazebo, PX4 and CUDA, and the simulation training process of MAV 3D visual navigation is designed. And we propose a method for judging whether the MAV pass the obstacles.
- We compare and discuss the navigation performances of various spiking network training frameworks (STBP, BPTT, SLAYER) and various time steps in detail. The experiment results show that HDDPG-STBP has higher success rate than original DDPG.

The rest of this paper is organized as follows: First, related work is presented in Section II. Then, the overall framework and pipeline of our algorithm are described in Section III, where the simulation system, HDDPG algorithm, and network training process are introduced in detail respectively. Next, the experimental results in the simulation environment are presented in Section IV. Finally, Section V summarizes the paper.

## II. RELATED WORK

Reinforcement learning aims to learn a policy through the interaction and feedback between agent and environment. By combining deep network with reinforcement learning, deep reinforcement learning algorithm arises. For example, the deep Q network (DQN) proposed by Mnih et al. [12] and the deep deterministic policy gradient (DDPG) proposed by Lillicrap et al. [13]. In recent years, it has become popular to apply deep reinforcement learning to visual autonomous navigation task of mobile robots. For instance, Tai et al. [14] firstly deployed DQN on wheeled robot based on a RGB-D camera and controlled the robot to explore autonomously in a simulation corridor environment by discrete actions. Aiming at the problems of overestimation of Q value and slow convergence of training in DQN, Xie et al. [15] proposed dueling double DQN (D3QN) algorithm, which realized twice accelerated training, and deployed it to an actual wheeled robot to realize autonomous exploration. Since DQN and its variants can not output continuous control variables, it is difficult to achieve higher control accuracy. Tai et al. [16] further proposed asynchronous DDPG algorithm, which uses 2D laser sensors to realize point-to-point autonomous navigation on virtual and actual wheeled robots. To collect training data faster, a separate thread is used for data collection. Furthermore, Mirowski et al. [17] used asynchronous advantage actor-critic (A3C) algorithm [18] as a training framework to realize the navigation of agents carrying a RGB camera in a 3D maze. They added two auxiliary tasks (deep prediction and closed-loop prediction) and took the loss of auxiliary tasks as additional supervision signals, which significantly improved the data efficiency and task performance when training agents. In addition, unlike point-to-point autonomous navigation tasks, Zhu et al. [19] proposed a target-driven visual deep reinforcement learning method. They extract features from the input target image and the image of the robot's view, projecting them to the same embedded space, and complete autonomous navigation by distinguishing the spatial relationship between the current state and the target.

All the above works were realized on wheeled robots, and later some works deployed on unmanned aerial vehicles appeared. Grando et al. [20] implemented mapless autonomous navigation of MAV using DDPG and soft actor-critic (SAC) [21] respectively. However, due to the use of 2D laser sensors, the MAV's movement is limited to 2D plane. They subsequently introduced recurrent neural network into the twin delayed deep deterministic policy gradient (TD3) algorithm to realize map-free navigation and obstacle avoidance of MAV [22]. Wang et al. [23] formulates the MAV navigation problem as partially observable Markov decision process, and proposed fast recursive deterministic policy gradient (Fast-RDPG) algorithm, which successfully enabled MAV to complete autonomous navigation at a fixed speed and altitude. In order to solve the sparse reward problem in reinforcement learning, they introduced a prior policy and achieved better navigation performance than using sparse reward directly for training [24]. He et al. [25] used a depth camera combined with DDPG to realize autonomous navigation of MAV in

<sup>1</sup>Supplementary Material: An accompanying video for this work is available at <https://youtu.be/P1GF0x9mWTU>.

3D environment, and the success rate achieved about 75% in simulation environments, and also verified the effectiveness of its method in real environments. Lee et al. [26] introduced hindsight experience replay mechanism [27] into SAC algorithm, adding reward feedback of state, action and target to MAV during training, which improved the learning speed and success rate. In this paper, we use neuromorphic reinforcement learning method to realize the visual autonomous navigation of MAV in the 3D environment for the first time, and achieve a comparable success rate.

### III. METHODOLOGY

In this section, we will describe the network architecture of the proposed neuromorphic reinforcement learning method for MAV 3D autonomous navigation (Neuro-Planner) in detail, including the various parts of our framework, procedures of network training, and components of simulation system.

#### A. Problem and Pipeline

1) *Problem Formulation*: This paper mainly focuses on the mapless autonomous navigation and local obstacle avoidance of MAV from a specified starting point to a goal point in 3D structured environment, where MAV only relies on its onboard state estimation and visual observations. Therefore, the point-to-point 3D visual autonomous navigation problem of MAV can be formally defined as follows. In a specified 3D environment, the starting point  $\mathbf{P}_{\text{start}} = [x_0, y_0, z_0]^\top$  and the goal point  $\mathbf{P}_{\text{goal}} = [x_*, y_*, z_*]^\top$  are given. Knowing the current position  $\mathbf{P}_k = [x_k, y_k, z_k]^\top$ , current velocity  $\mathbf{v}_k = [v_{xy,k}, v_{yaw,k}, v_{z,k}]^\top$  of the MAV and visual observation  $\mathbf{D}_k$  of onboard depth camera in the current step  $k$ , we can solve for current setting velocity command  $\bar{\mathbf{v}}_k = [\bar{v}_{xy,k}, \bar{v}_{yaw,k}, \bar{v}_{z,k}]^\top$  of MAV. Among them,  $v_{xy,k}$ ,  $v_{yaw,k}$ ,  $v_{z,k}$  are current horizontal linear velocity, horizontal angular velocity and vertical linear velocity of MAV respectively. MAV can reach the end point  $\mathbf{P}_{\text{end}} = [x_K, y_K, z_K]^\top$  near the specified goal point  $\mathbf{P}_{\text{goal}}$  from the starting point  $\mathbf{P}_{\text{start}}$  within a limited number of steps  $K$  ( $k = 1, \dots, K$ ) according to the actions, so that the Euclidean distance between the end point and the goal point is less than the setting threshold, that is,  $d_{\text{euclid}}(\mathbf{P}_{\text{end}}, \mathbf{P}_{\text{goal}}) < \varepsilon_{\text{goal,th}}$ . To this purpose, we need to design a navigation policy that infers the current action based on the current state to perform the task of 3D visual autonomous navigation. The specific algorithm pipeline is described as follows.

2) *Algorithm Pipeline*: The proposed Neuro-Planner is combined of deep reinforcement learning and spiking neural network. The implementation process of the algorithm can be roughly divided into the following two parts:

- **Hybrid Reinforcement Training**. We propose a hybrid actor-critic network architecture for neuromorphic reinforcement learning for MAV 3D visual autonomous navigation. Here, we use a spiking neuron-based MLP network to form an actor network. Firstly, the current state (position, velocity and visual features) is normalized and spiking encoded, and then spike trains of the state are sent to the spiking actor network to obtain spike trains of the action, which are then decoded into the

current action. In addition, a critic network (a deep MLP network) evaluates the current state and action. We use the hybrid deep deterministic policy gradient (HDDPG) algorithm to train the entire actor-critic networks.

- **Spiking Network Inference**. We only use the trained spiking actor network for action inference. Firstly, we normalize and spike the real-time state, and feed the spike trains of the state to the spiking neural network to get the spiking trains of the action in real time. We then decode it to the speed control command to realize 3D visual autonomous navigation of the MAV.

For systematic discussion, we first introduce the spiking network inference, followed by the hybrid reinforcement training.

#### B. Spiking Network Inference

We design a spiking actor network (SAN)  $f_{\text{SAN}}(\cdot)$ , which infers the output spike trains from the input spike trains and decodes them into an output action to complete the mapping from the state space to the action space.

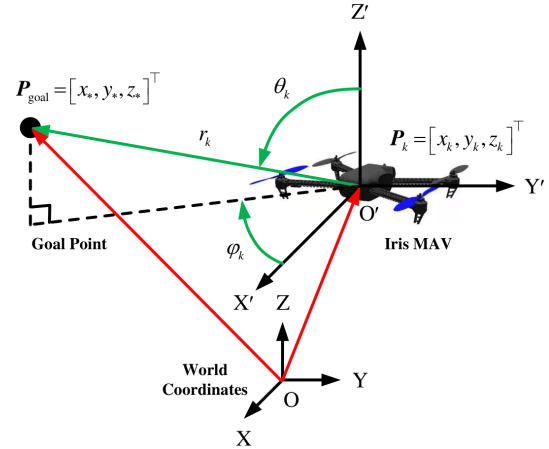


Fig. 2. Spherical coordinate system between the MAV and goal point.

1) *State and Action Selection*: For state space, the current state is composed of the relative position between MAV and goal point, the velocity of the MAV and the visual features of the depth camera. First, in order to express the relative positional relationship between the current position  $\mathbf{P}_k = [x_k, y_k, z_k]^\top$  of the MAV and the goal point  $\mathbf{P}_{\text{goal}} = [x_*, y_*, z_*]^\top$ , we use the current position of the MAV  $\mathbf{P}_k$  as the origin to establish a local spherical coordinate system to obtain the spherical coordinates of the goal point  $[r_k, \theta_k, \varphi_k]^\top$ , where  $r_k \in \mathbb{R}^+$  is the radial distance,  $\theta_k \in [0, \pi]$  is the polar angle, and  $\varphi_k \in [-\pi, \pi]$  is the azimuth angle, as shown in Fig 2. The x-y plane linear velocity and angular velocity of the MAV in the global coordinate system are  $v_{xy,k}$  and  $v_{yaw,k}$  respectively, and the z-axis linear velocity is  $v_{z,k}$ . In addition, since the depth image of the depth camera  $\mathbf{D}_k$  is a high-dimensional tensor, it is necessary to extract visual features from it. We use the pooling operation  $f_{\text{AP}}(\cdot)$  to divide the depth map into several image patches and calculate the average depth of effective pixels in each patch as visual features:

$$\mathbf{d}_k = f_{\text{AP}}(\mathbf{D}_k). \quad (1)$$

Compared with using the convolutional network to extract features, directly using pooling operation can effectively stabilize training and save memory. Therefore, the state at step  $k$  can be summarized as  $\mathbf{s}_k = [r_k, \theta_k, \varphi_k, v_{xy,k}, v_{yaw,k}, v_{z,k}, \mathbf{d}_k]^\top$ . For the action space, we map the current action  $\mathbf{a}_k$  output by the spiking actor network  $\mathbf{f}_{\text{SAN}}(\phi)$  to the setting velocity  $\bar{\mathbf{v}}_k = [\bar{v}_{xy,k}, \bar{v}_{yaw,k}, \bar{v}_{z,k}]^\top$ , and use the speed control method to control the MAV.

2) *State Normalization and Uniform Encoding*: Since the value range of each element in the current state  $\mathbf{s}_k$  is different, it needs to be normalized. Here, for elements in the state with bipolarity, we use dual channels to represent its positive and negative polarities respectively (since we use unipolar spiking neurons). In this way, the normalized current state is expressed as  $\tilde{\mathbf{s}}_k = [\tilde{r}_k, \tilde{\theta}_k, \tilde{\varphi}_k, \tilde{v}_{xy,k}, \tilde{v}_{yaw,k}, \tilde{v}_{z,k}, \tilde{\mathbf{d}}_k]^\top \in [0, 1]$ , and the specific normalization for each element is as follows:

$$\begin{aligned} \tilde{r}_k &= \frac{r_{\min}}{r_k}, \\ \tilde{\theta}_k &= \frac{\theta_k}{\pi}, \\ \tilde{\varphi}_k &= \begin{cases} \left[ \frac{|\varphi_k|}{\pi}, 0 \right]^\top, & \varphi_k \geq 0 \\ \left[ 0, \frac{|\varphi_k|}{\pi} \right]^\top, & \varphi_k < 0 \end{cases}, \\ \tilde{v}_{xy,k} &= \frac{v_{xy,k}}{v_{xy\text{-max}}}, \\ \tilde{v}_{yaw,k} &= \begin{cases} \left[ \frac{|v_{yaw,k}|}{v_{yaw\text{-max}}}, 0 \right]^\top, & v_{yaw,k} \geq 0 \\ \left[ 0, \frac{|v_{yaw,k}|}{v_{yaw\text{-max}}} \right]^\top, & v_{yaw,k} < 0 \end{cases}, \\ \tilde{v}_{z,k} &= \begin{cases} \left[ \frac{|v_{z,k}|}{v_{z\text{-max}}}, 0 \right]^\top, & v_{z,k} \geq 0 \\ \left[ 0, \frac{|v_{z,k}|}{v_{z\text{-max}}} \right]^\top, & v_{z,k} < 0 \end{cases}, \\ \tilde{\mathbf{d}}_k &= \frac{d_{\min}}{d_k}, \end{aligned} \quad (2)$$

where  $r_{\min} = 0.3$ ,  $v_{xy\text{-max}} = 0.5$ ,  $d_{\min} = 0.5$ ,  $v_{yaw\text{-max}} = 2$ ,  $v_{z\text{-max}} = 0.2$ . The length of the entire normalized state  $\tilde{\mathbf{s}}_k$  is  $C_{\tilde{\mathbf{s}}} = 21$ . In addition, since the spiking network deals with spike signals, we use uniform coding to encode the normalized state  $\tilde{\mathbf{s}}_k$  into a set of spike trains. According to the time step  $T$ , the generated spike array  $\mathbf{O}_{in,k}$  is represented as follows:

$$\mathbf{O}_{in,k}^t[i] = \begin{cases} 1, & \tilde{\mathbf{s}}_k[i] > \mathbf{M}_{\text{rand}}[i, t] \\ 0, & \text{otherwise} \end{cases}, \quad (3)$$

where  $\mathbf{M}_{\text{rand}}$  is a uniformly distributed random matrix of  $C_{\tilde{\mathbf{s}}} \times T$  size, whose element satisfies  $\mathbf{M}_{\text{rand}}[i, t] \sim U(0, 1)$ . We denote the above state normalization and spike encoding procedures as  $\mathbf{O}_{in,k} = \mathbf{f}_{\text{EC}}(\mathbf{s}_k, T) \doteq \mathbf{f}_{\text{EC}}(\mathbf{s}_k)$ .

3) *Spiking Actor Network*: We process the encoded spike trains using the spiking actor network (SAN), which is a spiking fully connected network (SFCN) of  $N$  layers. Its input is a spike array  $\mathbf{O}_{in,k}$  which is normalized and spike-encoded from the current state  $\mathbf{s}_k$ , and its output  $\mathbf{O}_{out,k}$  is a spike array (decoded into the current action  $\mathbf{a}_k$ ), expressed as follows:

$$\mathbf{O}_{out,k} = \mathbf{f}_{\text{SAN}}(\mathbf{O}_{in,k} | \phi). \quad (4)$$

For the specific implementation of each layer in the spiking actor network  $\mathbf{f}_{\text{SAN}}(\phi)$ , we use the two-state leaky integrate-and-fire (TS-LIF) spiking neuron model, which is a variant of the LIF neuron model [28]. The iterative update equation for the layer  $n \in [1, N]$  is given by:

$$\begin{aligned} \mathbf{C}_n^t &= \delta_{\text{curr},n} \mathbf{C}_n^{t-1} + \mathbf{W}_n \mathbf{O}_{n-1}^t + \mathbf{b}_n, \\ \mathbf{U}_n^t &= \delta_{\text{volt},n} \mathbf{U}_n^{t-1} \mathbf{g}(\mathbf{O}_n^{t-1}) + \mathbf{C}_n^t, \\ \mathbf{O}_n^t &= \mathbf{h}(\mathbf{U}_n^t). \end{aligned} \quad (5)$$

where  $t \in [1, T]$  denotes the discrete time,  $\mathbf{O}_1^t = \mathbf{O}_{in,k}^t$  is the input spike trains,  $\mathbf{O}_{out,k}^t = \mathbf{O}_N^t$  is the output spike trains,  $\mathbf{W}_n$  is the synaptic weight matrix,  $\mathbf{b}_n$  is the synaptic bias vector.  $\mathbf{C}_n^t$  and  $\mathbf{U}_n^t$  are the membrane current and membrane voltage respectively.  $\delta_{\text{curr},n}$  and  $\delta_{\text{volt},n}$  are the decay coefficients of the current and voltage respectively.  $\mathbf{g}(\mathbf{O}_n^{t-1}) = \mathbf{1} - \mathbf{O}_n^{t-1}$  is the reset gate.  $\mathbf{h}(\mathbf{U}_n^t) = \mathbf{H}(\mathbf{U}_n^t - u_{\text{th},n})$  is the fire gate.  $u_{\text{th},n}$  is the spike-triggered threshold. This iterative update equation incorporates all behaviors (integration, firing, decay, and reset) of TS-LIF neurons. It can be seen that different from the activation functions of analog neurons such as ReLU, TS-LIF spiking neurons have obvious time dependencies. Finally, we use a spike count (SC) layer to decode the output spike array  $\mathbf{O}_{out,k}$  to get the frequency of spikes as the action  $\mathbf{a}_k$  of the SAN output:

$$\mathbf{a}_k = \frac{1}{T} \sum_{t=1}^T \mathbf{O}_{out}^t, \quad (6)$$

where  $\mathbf{a}_k[i] \in [0, 1]$ . We denote the above spike decoding as  $\mathbf{a}_k = \mathbf{f}_{\text{DC}}(\mathbf{O}_{out,k}, T) \doteq \mathbf{f}_{\text{DC}}(\mathbf{O}_{out,k})$ .

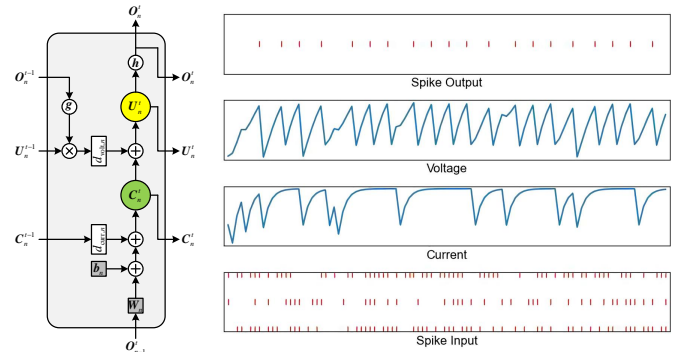


Fig. 3. Two-state leaky integrate-and-fire (TS-LIF) spiking neuron model. Different from analog neurons such as ReLU, since TS-LIF contains two states of current and voltage, it has rich spatio-temporal dynamics.

4) *Setting Velocity Mapping*: The current action  $\mathbf{a}_k[i] \in [0, 1]$  needs to be mapped to an appropriate setting velocity. Since the output spike trains are not distributed uniformly in the time step  $T$ , in order to ensure that the training can converge, we need to make the horizontal angular velocity  $\bar{v}_{yaw,k}$  and vertical linear velocity  $\bar{v}_{z,k}$  distributed uniformly at the beginning of the training. Thus, we use the difference between two channels to calculate  $\bar{v}_{yaw,k}$  and  $\bar{v}_{z,k}$ . Therefore,

we use the current action  $\mathbf{a}_k$  with four channels to solve for three setting velocities. We map  $\mathbf{a}_k$  to get the setting velocities:

$$\begin{aligned}\bar{v}_{xy,k} &= \alpha_1 \cdot (\mathbf{a}_k[1] + \mathbf{a}_k[2]) + v_{\min}, \\ \bar{v}_{yaw,k} &= \alpha_2 \cdot (\mathbf{a}_k[2] - \mathbf{a}_k[1]), \\ \bar{v}_{z,k} &= \alpha_3 \cdot (\mathbf{a}_k[4] - \mathbf{a}_k[3]),\end{aligned}\quad (7)$$

where  $\alpha_1 = 0.225$ ,  $\alpha_2 = 1.8$  and  $\alpha_3 = 0.18$ .  $v_{\min} = 0.05$  is the minimum horizontal linear velocity that enables the MAV to explore.

---

### Algorithm 1 SAN Forward Propagation

---

**Input:** State  $s_k$ .

Weights  $\mathbf{W}_n$  and biases  $\mathbf{b}_n$ .

Maximum time step T.

Network depth N.

Minimum plane linear velocity  $v_{\min}$ .

Velocity mapping factor  $\alpha_1, \alpha_2, \alpha_3$ .

**Output:** Setting velocity of MAV  $\bar{\mathbf{v}}_k = [\bar{v}_{xy,k}, \bar{v}_{yaw,k}, \bar{v}_{z,k}]^\top$ .

- 1: Normalize and uniformly encode the state  $s_k$  to get the input spike train  $\mathbf{O}_{in,k} = \mathbf{f}_{EC}(s_k)$ .
  - 2: Propagate SAN with time  $t$  and layer  $n$  recurrently:
  - 3: **for**  $t = 1, \dots, T$  **do**
  - 4:    $\mathbf{O}_1^t = \mathbf{O}_{in,k}^t$ .
  - 5:   **for**  $l = 1, \dots, L$  **do**
  - 6:      $\mathbf{C}_n^t = \delta_{curr,n} \mathbf{C}_n^{t-1} + \mathbf{W}_n \mathbf{O}_{n-1}^t + \mathbf{b}_n$ .
  - 7:      $\mathbf{U}_n^t = \delta_{volt,n} \mathbf{U}_n^{t-1} g(\mathbf{O}_n^{t-1}) + \mathbf{C}_n^t$ .
  - 8:      $\mathbf{O}_n^t = h(\mathbf{U}_n^t)$ .
  - 9:   **end for**
  - 10:    $\mathbf{O}_{out,k}^t = \mathbf{O}_N^t$ .
  - 11: **end for**
  - 12: Decode the output spike train  $\mathbf{O}_{out,k}$  to get the action  $\mathbf{a}_k = \mathbf{f}_{DC}(\mathbf{O}_{out,k})$ .
  - 13: Map action  $\mathbf{a}_k$  to actual setting velocity  $\bar{\mathbf{v}}_k$ :
  - 14:  $\bar{v}_{xy,k} = \alpha_1 \cdot (\mathbf{a}_k[1] + \mathbf{a}_k[2]) + v_{\min}$ .
  - 15:  $\bar{v}_{yaw,k} = \alpha_2 \cdot (\mathbf{a}_k[2] - \mathbf{a}_k[1])$ .
  - 16:  $\bar{v}_{z,k} = \alpha_3 \cdot (\mathbf{a}_k[4] - \mathbf{a}_k[3])$ .
- 

### C. Hybrid Reinforcement Training

For the spiking actor network (SAN)  $\mathbf{f}_{SAN}(\phi)$  to learn an appropriate navigation policy, we employ the reinforcement learning paradigm. In this paper, we propose a neuromorphic reinforcement learning method (HDDPG) based on the deep deterministic policy gradient (DDPG) algorithm [13] as the training framework.

#### 1) Hybrid Deep Deterministic Policy Gradient (HDDPG):

The DDPG algorithm is a deep reinforcement learning framework that can effectively optimize the expected return and estimate value function. On the basis of the DDPG [13] algorithm, our proposed hybrid deep deterministic policy gradient (HDDPG) algorithm combining the SNN dynamics and actor-critic network architecture, as shown in Fig. 4. First,  $\mathbf{f}_{SAN}(\phi)$  maps the current state  $s_k$  to the current action  $\mathbf{a}_k(s_k | \phi)$  with its encoding function  $\mathbf{f}_{EC}(\cdot)$  and decoding function  $\mathbf{f}_{DC}(\cdot)$ . In order to improve the robustness of the policy, we add random noises  $\kappa$  to the output of  $\mathbf{f}_{SAN}(\phi)$  in the training phase, and get:

$$\mathbf{a}_k = \mathbf{f}_{DC}(\mathbf{f}_{SAN}(\mathbf{f}_{EC}(s_k) | \phi)) + \kappa. \quad (8)$$

Then, the deep critic network (DCN)  $f_{DCN}(\psi)$  formed by the deep network evaluates  $s_k$  and  $\mathbf{a}_k$  output by  $\mathbf{f}_{SAN}(\phi)$ , and obtains the Q value  $Q_k$ :

$$Q_k = f_{DCN}(s_k, \mathbf{a}_k | \psi). \quad (9)$$

In other words,  $\mathbf{f}_{SAN}(\phi)$  aims to find appropriate  $\mathbf{a}_k$ , which maximizes  $Q_k$  of  $f_{DCN}(\psi)$ . In addition, we adopt the experience replay mechanism [12] to improve the data utilization during training, as shown in Fig. 4(a). The current state  $s_k$ , the current action  $\mathbf{a}_k$ , the next state  $s_{k+1}$ , the reward  $r_k$  from the state transition and the current episode end flag  $\varepsilon_k$  are stored in the experience replay buffer as a transition, so that MAV can improve the current policy from the previous experience. At the same time, in order to make the networks converge stably, we use the target network mechanism [12] to set the conventional networks and the target networks respectively, as shown in Fig. 4(b). The parameters of the conventional networks are updated at each backpropagation. The parameters of target networks are frozen and only updated when the set number of backpropagations is reached. Here, target spiking actor network (TSAN)  $\mathbf{f}_{TSAN}(\phi')$  and the target deep critic network (TDCN)  $f_{TDCN}(\psi')$  are set. We sample B experiences  $\{s_i, \mathbf{a}_i, s_{i+1}, r_i, \varepsilon_i\}$  from the experience replay buffer  $\mathbf{R}$  for batch training. First,  $f_{DCN}(\psi)$ ,  $f_{TDCN}(\psi')$  and the reward  $r_k$  are used to construct temporal-difference (TD) loss function, which is expressed as follows:

$$\begin{aligned}L_{TD}(\psi) &= [r_i + \gamma Q_{i+1} \cdot (1 - \varepsilon_i) - Q_i]^2, \\ Q_{i+1} &= f_{TDCN}(s_{i+1}, \mathbf{a}_{i+1} | \psi') \\ &= f_{TDCN}(s_{i+1}, \mathbf{f}_{DC}(\mathbf{f}_{TSAN}(\mathbf{f}_{EC}(s_{i+1}) | \phi')) | \psi'), \\ Q_i &= f_{DCN}(s_i, \mathbf{a}_i | \psi).\end{aligned}\quad (10)$$

where  $\gamma$  is the discount factor. Then, the Q value can be directly used as its loss function for  $\mathbf{f}_{SAN}(\phi)$ , which is expressed as follows:

$$\begin{aligned}L_Q(\phi) &= -Q'_i \\ &= -f_{DCN}(s_i, \mathbf{f}_{DC}(\mathbf{f}_{SAN}(\mathbf{f}_{EC}(s_i)) | \phi) | \psi).\end{aligned}\quad (11)$$

In addition, the parameters of  $\mathbf{f}_{TSAN}(\phi')$  and  $f_{TDCN}(\psi')$  are periodically soft-updated by the parameters of  $\mathbf{f}_{SAN}(\phi)$  and  $f_{DCN}(\psi)$  to improve the stability of the learning process, which is specifically expressed as follows:

$$\begin{aligned}\phi' &= \eta \phi + (1 - \eta) \phi', \\ \psi' &= \eta \psi + (1 - \eta) \psi',\end{aligned}\quad (12)$$

where is  $\eta$  a sufficiently small constant. For the reward function  $r_k$ , its specific form is as follows:

$$r_k = \begin{cases} r_{\text{goal}} & \text{if } d_{\text{euclid}}(\mathbf{P}_k, \mathbf{P}_{\text{goal}}) < \varepsilon_{\text{goal,th}} \\ r_{\text{obs}} & \text{if } d_{\text{euclid}}(\mathbf{P}_k, \mathbf{P}_{\text{obs}}) < \varepsilon_{\text{obs,th}} \\ r_{\text{other}} & \text{otherwise} \end{cases}, \quad (13)$$

$$r_{\text{other}} = \sigma \cdot (d_{\text{euclid}}(\mathbf{P}_k, \mathbf{P}_{\text{goal}}) - d_{\text{euclid}}(\mathbf{P}_{k-1}, \mathbf{P}_{\text{goal}})).$$

where  $r_{\text{goal}}$  and  $r_{\text{obstacle}}$  are the positive and negative rewards respectively.  $d_{\text{euclid}}(\mathbf{P}_k, \mathbf{P}_{\text{goal}})$  is the distance to the goal point,  $d_{\text{euclid}}(\mathbf{P}_k, \mathbf{P}_{\text{obs}})$  is the distance to the nearest obstacle,  $\sigma$  is the amplification factor,  $\varepsilon_{\text{goal,th}}$  and  $\varepsilon_{\text{obs,th}}$  are the distance threshold to the goal point and the distance threshold to the obstacle

respectively. In a word,  $r_k$  is designed to guide the MAV to move towards the goal and avoid obstacles during autonomous navigation.

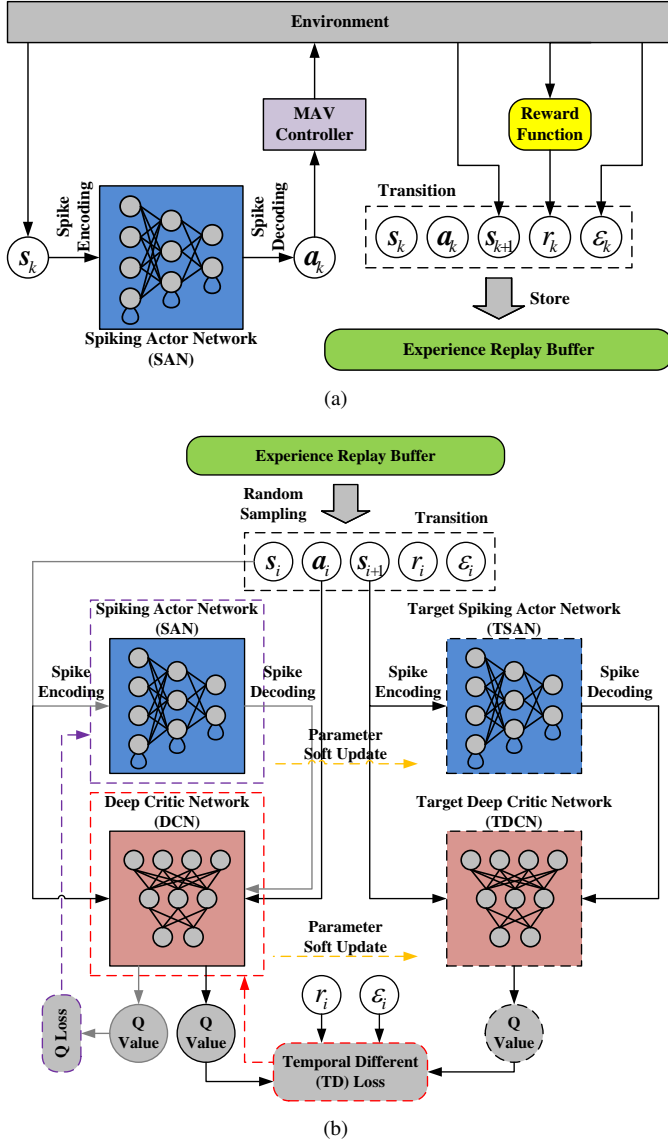


Fig. 4. Overview of the proposed hybrid deep deterministic policy gradient (HDDPG) algorithm. (a) Experience replay mechanism [12]. (b) Temporal different (TD) loss and Q loss.

2) *Spatio-Temporal Back Propagation (STBP) for TS-LIF-based SAN*: In our HDDPG algorithm,  $f_{DCN}(\psi)$  is directly trained using the conventional back-propagation algorithm.  $f_{SAN}(\phi)$  has the characteristics of space-time dynamics and has the issue that the spike function is not differentiable. For  $f_{SAN}(\phi)$  based on TS-LIF spiking neurons, we train it using our improved spatio-temporal back-propagation (STBP) [29]. According to Eq. (5) and Eq. (11), the parameters that  $f_{SAN}(\phi)$  finally needs to update are the weights  $\mathbf{W}_n$  and the biases  $\mathbf{b}_n$ , so we need to obtain the derivative of the loss  $L_Q$  with respect to  $\mathbf{W}_n$  and  $\mathbf{b}_n$ . According to Eq. (5), we expand  $f_{SAN}(\phi)$  with TS-LIF spiking neurons in the space and time directions to obtain two chains of spatial propagation and temporal propagation, and realize iterative

## Algorithm 2 HDDPG

**Input:** Spiking actor network  $f_{SAN}(\phi)$ .

Deep critic network  $f_{DCN}(\psi)$ .

Target network  $f_{TSAN}(\phi')$  and  $f_{TDCN}(\psi')$ .

**Output:** Temporal difference (TD) loss  $L_{TD}(\psi)$  and Q loss  $L_Q(\phi)$ .

- 1: Randomly initialize spiking actor network  $f_{SAN}(\phi)$  and deep critic network  $f_{DCN}(\psi)$  with weights  $\phi$  and  $\psi$ .
- 2: Initialize target network  $f_{TSAN}(\phi')$  and  $f_{TDCN}(\psi')$  with weights  $\phi' \leftarrow \phi$  and  $\psi' \leftarrow \psi$ .
- 3: Initialize replay buffer  $\mathbf{R}$ .
- 4: **for**  $m = 1, \dots, M$  **do**
- 5:   Receive initial pbservation state  $\mathbf{s}_0$ .
- 6:   **for**  $k = 1, \dots, K$  **do**
- 7:     Select action  $\mathbf{a}_k = f_{DC}(f_{SAN}(f_{EC}(\mathbf{s}_k)|\phi)) + \kappa$  according to the current policy and exploration noise.
- 8:     Execute action  $\mathbf{a}_k$ , and get reward  $r_k$ , new state  $\mathbf{s}_{k+1}$  and epoch end bit  $\epsilon_k$ .
- 9:     Store current transition  $[\mathbf{s}_k, \mathbf{a}_k, r_k, \mathbf{s}_{k+1}, \epsilon_k]^\top$  in experience replay buffer  $\mathbf{R}$ .
- 10:    Sample a random minibatch of  $N$  transitions  $[\mathbf{s}_i, \mathbf{a}_i, r_i, \mathbf{s}_{i+1}, \epsilon_i]^\top$  from experience replay buffer  $\mathbf{R}$ .
- 11:    Update critic by minimizing TD error loss:  
 $L_{TD}(\psi) = [r_i + \gamma Q_{i+1} \cdot (1 - \epsilon_i) - Q_i]^2$ .
- 12:    Update action with maximum Q loss:  
 $L_Q(\phi) = -Q'_i$ .
- 13:    Update target networks:  
 $\phi' = \eta\phi + (1 - \eta)\phi'$ ,  $\psi' = \eta\psi + (1 - \eta)\psi'$ .
- 14:    **end for**
- 15: **end for**

forward propagation. In the propagation chains,  $\mathbf{W}_n$  and  $\mathbf{b}_n$  are included in the current recurrence relation, so we calculate the derivative of the loss  $L_Q$  to the currents  $\mathbf{C}_n^t$  of the current layer  $n$  at time  $t$ , and we can further calculate the derivative of  $L_Q$  with respect to  $\mathbf{W}_n$  and  $\mathbf{b}_n$ . According to Eq. (6) and Eq. (11), the derivative of  $L_Q$  with respect to the action  $\mathbf{a}$  can be directly obtained according to the back-propagation of  $f_{DCN}(\psi)$ :

$$\frac{\partial L_Q}{\partial \mathbf{a}} = -\frac{\partial Q}{\partial \mathbf{a}} = -\frac{\partial f_{DCN}(\mathbf{s}, \mathbf{a})}{\partial \mathbf{a}}. \quad (14)$$

According to Eq. (5), in order to obtain the derivative of  $L_Q$  to the spikes  $\mathbf{O}_n^t$ , the voltages  $\mathbf{U}_n^t$ , and the currents  $\mathbf{C}_n^t$ , it can be divided into the following four cases depending on the layer  $n$  and time  $t$ :

Case 1: At the time  $t = T$  and the output layer  $n = N$ . In this case, only spatial derivatives exists. The derivative of  $L_Q$  with respect to  $\mathbf{O}_N^T$  is obtained by dividing the derivative of  $L_Q$  with respect to  $\mathbf{a}$  equally over each time:

$$\frac{\partial L_Q}{\partial \mathbf{O}_N^T} = \frac{\partial L_Q}{\partial \mathbf{O}_N^T} \Big|_{\text{spatial}} = \frac{\partial L_Q}{\partial \mathbf{a}} \frac{\partial \mathbf{a}}{\partial \mathbf{O}_N^T} = \frac{1}{T} \frac{\partial L_Q}{\partial \mathbf{a}}. \quad (15)$$

The derivative of  $L_Q$  with respect to  $U_N^T$  depends only on the derivative of  $L_Q$  with respect to  $O_N^T$ :

$$\frac{\partial L_Q}{\partial U_N^T} = \frac{\partial L_Q}{\partial U_N^T} \Big|_{\text{spatial}} = \frac{\partial L_Q}{\partial O_N^T} \frac{\partial O_N^T}{\partial U_N^T} = \frac{\partial L_Q}{\partial O_N^T} \dot{\mathbf{h}}(U_N^T). \quad (16)$$

The derivative of  $L_Q$  with respect to  $C_N^T$  depends only on the derivative of  $L_Q$  with respect to  $U_N^T$ :

$$\frac{\partial L_Q}{\partial C_N^T} = \frac{\partial L_Q}{\partial C_N^T} \Big|_{\text{spatial}} = \frac{\partial L_Q}{\partial U_N^T} \frac{\partial U_N^T}{\partial C_N^T} = \frac{\partial L_Q}{\partial U_N^T}. \quad (17)$$

Case2: At the time  $t = T$  and the middle layer  $n < N$ . In this case, only spatial derivatives exists, recursively depending on error propagation in the spatial domain at time T. The derivative of  $L_Q$  with respect to  $O_n^T$  depends only on the derivative of  $L_Q$  with respect to  $C_{n+1}^T$ :

$$\frac{\partial L_Q}{\partial O_n^T} = \frac{\partial L_Q}{\partial O_n^T} \Big|_{\text{spatial}} = \frac{\partial L_Q}{\partial C_{n+1}^T} \frac{\partial C_{n+1}^T}{\partial O_n^T} = \frac{\partial L_Q}{\partial C_{n+1}^T} \mathbf{W}_n. \quad (18)$$

The derivative of  $L_Q$  with respect to  $U_n^T$  depends only on the derivative of  $L_Q$  with respect to  $O_n^T$ :

$$\frac{\partial L_Q}{\partial U_n^T} = \frac{\partial L_Q}{\partial U_n^T} \Big|_{\text{spatial}} = \frac{\partial L_Q}{\partial O_n^T} \frac{\partial O_n^T}{\partial U_n^T} = \frac{\partial L_Q}{\partial O_n^T} \dot{\mathbf{h}}(U_n^T). \quad (19)$$

The derivative of  $L_Q$  with respect to  $C_n^T$  depends only on the derivative of  $L_Q$  with respect to  $U_n^T$ :

$$\frac{\partial L_Q}{\partial C_n^T} = \frac{\partial L_Q}{\partial C_n^T} \Big|_{\text{spatial}} = \frac{\partial L_Q}{\partial U_n^T} \frac{\partial U_n^T}{\partial C_n^T} = \frac{\partial L_Q}{\partial U_n^T}. \quad (20)$$

Case 3: At the time  $t < T$  and the output layer  $n = N$ . In this case, the derivative depends on both the temporal and spatial domain directions of error propagation. The derivative of  $L_Q$  with respect to  $O_N^t$  depends on both the derivative of  $L_Q$  with respect to  $\mathbf{a}$  in the space domain and the derivative of  $L_Q$  with respect to  $U_N^{t+1}$  in the time domain:

$$\begin{aligned} \frac{\partial L_Q}{\partial O_N^t} &= \frac{\partial L_Q}{\partial O_N^t} \Big|_{\text{spatial}} + \frac{\partial L_Q}{\partial O_N^t} \Big|_{\text{temporal}} \\ &= \frac{\partial L_Q}{\partial \mathbf{a}} \frac{\partial \mathbf{a}}{\partial O_N^t} + \frac{\partial L_Q}{\partial U_N^{t+1}} \frac{\partial U_N^{t+1}}{\partial O_N^t} \\ &= \frac{1}{T} \frac{\partial L_Q}{\partial \mathbf{a}} + \frac{\partial L_Q}{\partial U_N^{t+1}} \delta_{\text{volt},N} U_N^t \dot{\mathbf{g}}(O_N^t). \end{aligned} \quad (21)$$

The derivative of  $L_Q$  with respect to  $U_N^t$  depends on both the derivative of  $L_Q$  with respect to  $O_N^t$  in the space domain and the derivative of  $L_Q$  with respect to  $U_N^{t+1}$  in the time domain:

$$\begin{aligned} \frac{\partial L_Q}{\partial U_N^t} &= \frac{\partial L_Q}{\partial U_N^t} \Big|_{\text{spatial}} + \frac{\partial L_Q}{\partial U_N^t} \Big|_{\text{temporal}} \\ &= \frac{\partial L_Q}{\partial O_N^t} \frac{\partial O_N^t}{\partial U_N^t} + \frac{\partial L_Q}{\partial U_N^{t+1}} \frac{\partial U_N^{t+1}}{\partial U_N^t} \\ &= \frac{\partial L_Q}{\partial O_N^t} \dot{\mathbf{h}}(U_N^t) + \frac{\partial L_Q}{\partial U_N^{t+1}} \delta_{\text{volt},N} \mathbf{g}(O_N^t). \end{aligned} \quad (22)$$

The derivative of  $L_Q$  with respect to  $C_N^t$  depends both on the derivative of  $L_Q$  with respect to  $U_N^t$  in the space domain, and the derivative of  $L_Q$  with respect to  $C_N^{t+1}$  in the time domain:

$$\begin{aligned} \frac{\partial L_Q}{\partial C_N^t} &= \frac{\partial L_Q}{\partial C_N^t} \Big|_{\text{spatial}} + \frac{\partial L_Q}{\partial C_N^t} \Big|_{\text{temporal}} \\ &= \frac{\partial L_Q}{\partial U_N^t} \frac{\partial U_N^t}{\partial C_N^t} + \frac{\partial L_Q}{\partial C_N^{t+1}} \frac{\partial C_N^{t+1}}{\partial C_N^t} \\ &= \frac{\partial L_Q}{\partial U_N^t} + \frac{\partial L_Q}{\partial C_N^{t+1}} \delta_{\text{curr},N}. \end{aligned} \quad (23)$$

Case 4: At the time  $t < T$  and the middle layer  $n < N$ . In this case, the derivative depends on both the temporal and spatial domain directions of error propagation. The derivative of  $L_Q$  with respect to  $O_n^t$  depends on both the derivative of  $L_Q$  with respect to  $C_{n+1}^t$  in the space domain and the derivative of  $L_Q$  with respect to  $U_{n+1}^t$  in the time domain:

$$\begin{aligned} \frac{\partial L_Q}{\partial O_n^t} &= \frac{\partial L_Q}{\partial O_n^t} \Big|_{\text{spatial}} + \frac{\partial L_Q}{\partial O_n^t} \Big|_{\text{temporal}} \\ &= \frac{\partial L_Q}{\partial C_{n+1}^t} \frac{\partial C_{n+1}^t}{\partial O_n^t} + \frac{\partial L_Q}{\partial U_{n+1}^t} \frac{\partial U_{n+1}^t}{\partial O_n^t} \\ &= \frac{\partial L_Q}{\partial C_{n+1}^t} \mathbf{W}_{n+1} + \frac{\partial L_Q}{\partial U_{n+1}^t} \delta_{\text{volt},n} U_n^t \dot{\mathbf{g}}(O_n^t). \end{aligned} \quad (24)$$

The derivative of  $L_Q$  with respect to  $U_n^t$  depends on both the derivative of  $L_Q$  with respect to  $O_n^t$  in the space domain and the derivative of  $L_Q$  with respect to  $U_n^{t+1}$  in the time domain:

$$\begin{aligned} \frac{\partial L_Q}{\partial U_n^t} &= \frac{\partial L_Q}{\partial U_n^t} \Big|_{\text{spatial}} + \frac{\partial L_Q}{\partial U_n^t} \Big|_{\text{temporal}} \\ &= \frac{\partial L_Q}{\partial O_n^t} \frac{\partial O_n^t}{\partial U_n^t} + \frac{\partial L_Q}{\partial U_n^{t+1}} \frac{\partial U_n^{t+1}}{\partial U_n^t} \\ &= \frac{\partial L_Q}{\partial O_n^t} \dot{\mathbf{h}}(U_n^t) + \frac{\partial L_Q}{\partial U_n^{t+1}} \delta_{\text{volt},n} \mathbf{g}(O_n^t). \end{aligned} \quad (25)$$

The derivative of  $L_Q$  with respect to  $C_n^t$  depends both on the derivative of  $L_Q$  with respect to  $U_n^t$  in the space domain, and the derivative of  $L_Q$  with respect to  $C_n^{t+1}$  in the time domain:

$$\begin{aligned} \frac{\partial L_Q}{\partial C_n^t} &= \frac{\partial L_Q}{\partial C_n^t} \Big|_{\text{spatial}} + \frac{\partial L_Q}{\partial C_n^t} \Big|_{\text{temporal}} \\ &= \frac{\partial L_Q}{\partial U_n^t} \frac{\partial U_n^t}{\partial C_n^t} + \frac{\partial L_Q}{\partial C_n^{t+1}} \frac{\partial C_n^{t+1}}{\partial C_n^t} \\ &= \frac{\partial L_Q}{\partial U_n^t} + \frac{\partial L_Q}{\partial C_n^{t+1}} \delta_{\text{curr},n}. \end{aligned} \quad (26)$$

Based on the above four cases, we can get the derivative of  $L_Q$  to  $O_n^t$ ,  $U_n^t$ ,  $C_n^t$  at any layer  $n$  and any time  $t$ , and then get the derivative of  $L_Q$  to  $\mathbf{W}_n$  and  $\mathbf{b}_n$  as follows:

$$\begin{aligned} \frac{\partial L_Q}{\partial \mathbf{W}_n} &= \sum_{t=1}^T \frac{\partial L_Q}{\partial C_n^t} \frac{\partial C_n^t}{\partial \mathbf{W}_n} = \sum_{t=1}^T \frac{\partial L_Q}{\partial C_n^t} O_n^{t-1}, \\ \frac{\partial L_Q}{\partial \mathbf{b}_n} &= \sum_{t=1}^T \frac{\partial L_Q}{\partial C_n^t} \frac{\partial C_n^t}{\partial \mathbf{b}_n} = \sum_{t=1}^T \frac{\partial L_Q}{\partial C_n^t}, \end{aligned} \quad (27)$$

where  $\frac{\partial L_Q}{\partial C_n^t}$  can be obtained from Eq. (14) to Eq. (26). In addition, since the spike generating function  $\mathbf{h}(\cdot)$  of the TS-LIF spiking neurons is not differentiable, here we use the

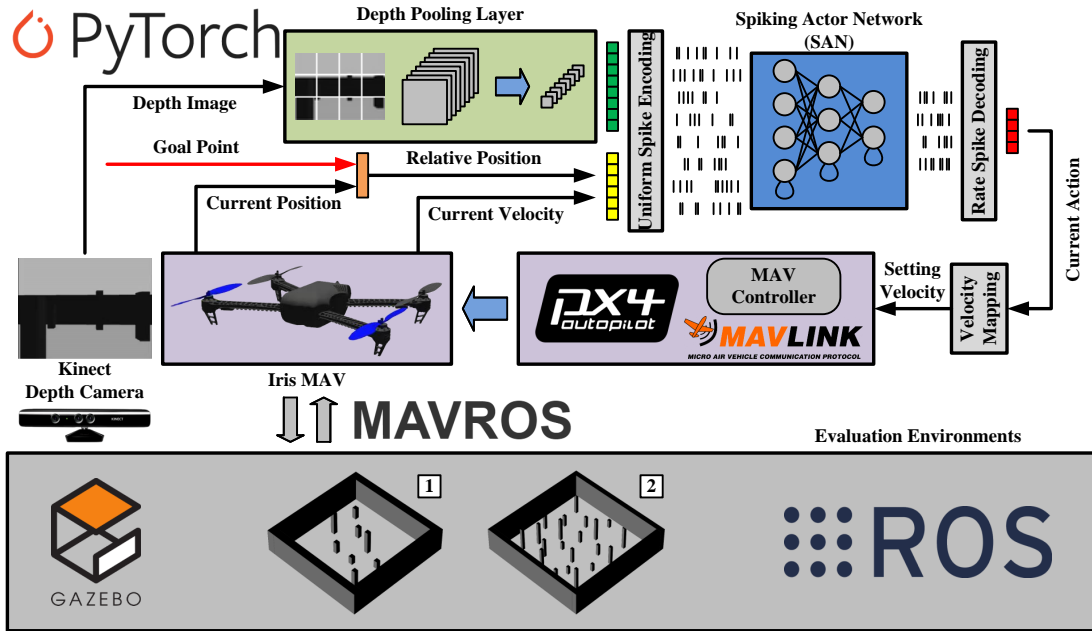


Fig. 5. MAV simulation system framework through the robot operating system (ROS).

rectangular function as the surrogate gradient function to approximate the derivative of  $h(\cdot)$ :

$$\dot{h}(U_n^t) = \frac{1}{m} \mathbf{H} \left( \frac{m}{2} - |U_n^t - u_{th,n}| \right). \quad (28)$$

Among them, coefficient  $m = 1.0$  and spike trigger threshold  $u_{th,n} = 0.5$ . Based on the STBP framework for the above TS-LIF spiking neurons, we can use gradient descent to efficiently train  $f_{SAN}(\phi)$ . In experiments, we also compare other two SNN training frameworks, back-propagation through time (BPTT) [30] and spike layer error reassignment (SLAYER) [31].

#### D. MAV Simulation System

1) *Software-in-the-Loop Simulation Framework*: In order to perform hybrid reinforcement training and spiking network inference in the simulation environment, we built a complete set of MAV software-in-the-loop (SITL) simulation system based on the Robot Operating System (ROS), as shown in Fig. 5. It mainly includes the following components:

- **Simulation Environment**. We use Gazebo<sup>2</sup> simulator to set up the training environment and the evaluation environment respectively. We learn the insight of curriculum learning and set up four training environments from simple to complex in total. In order to evaluate the generalization of our algorithm, we set up a total of two evaluation environments. Evaluation environment #1 is similar in size to the training environment, and Evaluation environment #2 is larger, more complex and more challenging.
- **MAV with Depth Camera**. In the Gazebo simulation framework, we choose the Iris MAV and the Kinect depth

camera, and the depth camera is fixed at  $(0, 0, 0.14\text{m})$  the MAV body.

- **Flight Control**. In order to realize the speed control of the MAV, we choose PX4<sup>3</sup> [32] as the flight controller of the MAV. PX4 is an open-source professional flight controller that supports a variety of MAV models and simulation platforms, providing a wealth of application programming interfaces (APIs) to facilitate the deployment of actual MAVs. It is widely used in the current robotics research community around the world.
- **Communication Mechanism**. We use ROS nodes for message interaction between algorithm programs, Gazebo simulation environment and PX4 flight controller.

2) *MAV Take-Off Process*: For the training or evaluation, the MAV takes off to a fixed altitude from a random starting point at the beginning of each episode. First, the MAV randomly appears in a specified starting point on the ground by the service in Gazebo. Then, the MAV switches to the off-board mode and enters the idle speed. Finally, the MAV flies to the fixed altitude to perform autonomous navigation after a period of time.

3) *Judgment of MAV over Obstacles*: During the training process, it is necessary to determine whether the MAV has pass the obstacle. We propose an appropriate judgment of MAV over obstacles as shown in Fig. 6. For obstacles lower than the MAV current height, it is considered that the MAV can pass directly. For obstacles higher than the MAV current height, the distance in xy-plane between the MAV and obstacle are calculated. If the distance between the MAV and the obstacle in xy-plane is less than the collision threshold, it is considered that the MAV has collided, otherwise the MAV is considered to pass the obstacle safely.

<sup>2</sup>Gazebo Website: <https://gazebo.org>.

<sup>3</sup>PX4 Website: <https://px4.io/>.

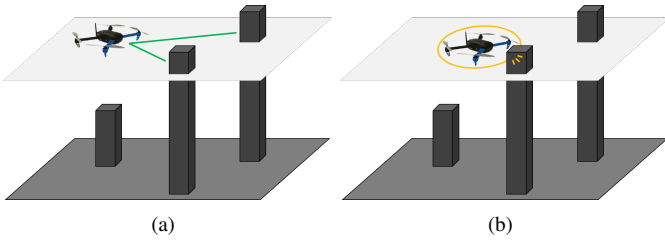


Fig. 6. Judgment of MAV over obstacles. (a) Only distance from obstacles higher than the current flight altitude is calculated. (b) If the distance between the MAV and the obstacle is less than the threshold, a collision is considered to have occurred.

#### IV. EXPERIMENTS

In this section, we conduct multiple experiments in the Gazebo simulation environments to verify the effectiveness of the Neuro-Planner proposed in this paper through qualitative and quantitative experimental results. First, we evaluate the impact of original DDPG and HDPG implemented by three different SNN training frameworks (STBP [29], BPTT [30], and SLAYER [31]) on the performance during training. Then, the success rate, average distances and average time of successful paths by different training frameworks are evaluated in two significantly different evaluation environments, and success and failure trajectories are shown finally. In the following part, we use HDPG-STBP, HDPG-BPTT, HDPG-SLAYER to represent HDPG algorithm trained with STBP, BPTT and SLAYER frameworks respectively.

##### A. Experiment Setup

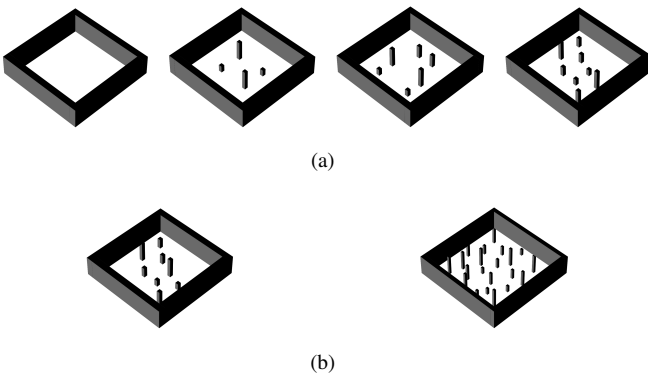


Fig. 7. Training and evaluation environments in Gazebo simulator. We adopt the insight of curriculum learning in setting training environments. (a) Training environments #1-#4: Four training environments ( $12\text{m} \times 12\text{m} \times 3\text{m}$ ) of increasing complexity with 0, 4, 6 and 8 cuboid pillars. [33] [34] [35]. (b) Evaluation environments #1-#2: Two evaluation environments. Evaluation environment #1 is similar to training environment #4, and evaluation environment #2 is  $20\text{m} \times 20\text{m} \times 3\text{m}$  with 21 cuboid pillars.

In this paper, we use a hybrid reinforcement training method based on curriculum learning [33] [34] [35] to train the actor-critic network. We set up a total of four training environments, sequentially increasing the difficulty of the environment to speed up training and improve performance, as shown in Fig. 7(a). Four training environments with a size of  $12\text{m} \times 12\text{m} \times 3\text{m}$

TABLE I  
HYPER-PARAMETERS FOR NEURO-PLANNER TRAINING

Parameters	Values
Channels of state $C_s$	18
Channels of normalized state $C_{\bar{s}}$	21
Channels of action $C_a$	4
Spike trigger threshold $u_{th,n}$	0.5
Decay factor of current $\delta_{curr,n}$	0.5
Decay factor of voltage $\delta_{volt,n}$	0.75
Velocity mapping factors $\alpha_1, \alpha_2, \alpha_3$	0.225, 1.8, 0.18
Minimum plane linear velocity $v_{min}$	0.05
Hidden layers of SAN	3
Hidden layers of DCN	3
Neurons in each hidden layer of SAN	512
Neurons in each hidden layer of DCN	512
Reward for reaching the goal point $r_{goal}$	30
Reward for collision with obstacle $r_{obs}$	-30
Amplified factor of rewards $\sigma$	15
Distance threshold to goal point $\varepsilon_{goal,th}$	0.54 m
Distance threshold to obstacle $\varepsilon_{obs,th}$	0.5 m
Learning rate of SAN	0.00001
Learning rate of DCN	0.0001
Sizes of experience replay buffer	100000
Soft update factor $\eta$	0.01
Batch size B	256
Height restrictions	0.3m, 3.1m

are set with closed walls as enclosures. In the four training environments, 0, 4, 6, and 8 cuboid pillars are placed as obstacles in sequence. The placements of obstacles in each training environment are shown in Fig. 7. In order to enable the MAV to fully learn the navigation policy, we set 100, 200, 300, and 400 training episodes in each training environment, and randomly generated starting points and goal points. The training parameters are shown in Table I.

For the evaluation environment, we set up two unfamiliar environments, as shown in Fig. 7(b). Evaluation environment #1 changes the height of some columns compared to training environment #4. To further verify the robustness of our Neuro-Planner, evaluation environment #2 is designed more complexity with  $20\text{m} \times 20\text{m} \times 3\text{m}$ . A total of 21 cuboid pillars are placed in evaluation environment #2 as obstacles. In each evaluation environment, we randomly generate 100 starting points and goal points for evaluation, and compare the performance of the spiking actor networks trained with different training frameworks and the artificial network. In order to ensure that the evaluation difficulty of each method is consistent, each method will use the same starting points and goal points. In the evaluation phase, we take the success rate as a priority condition. To exclude chance, we repeat the evaluation three times for each different training frameworks, and take the average success rate. Besides the success rate, we also calculated the average distance and average speed when each method successfully reached the goal point. Both training and evaluation in our experiments are performed under Ubuntu 18.04, using Gazebo9 as the simulator. The CPU is Intel i7-

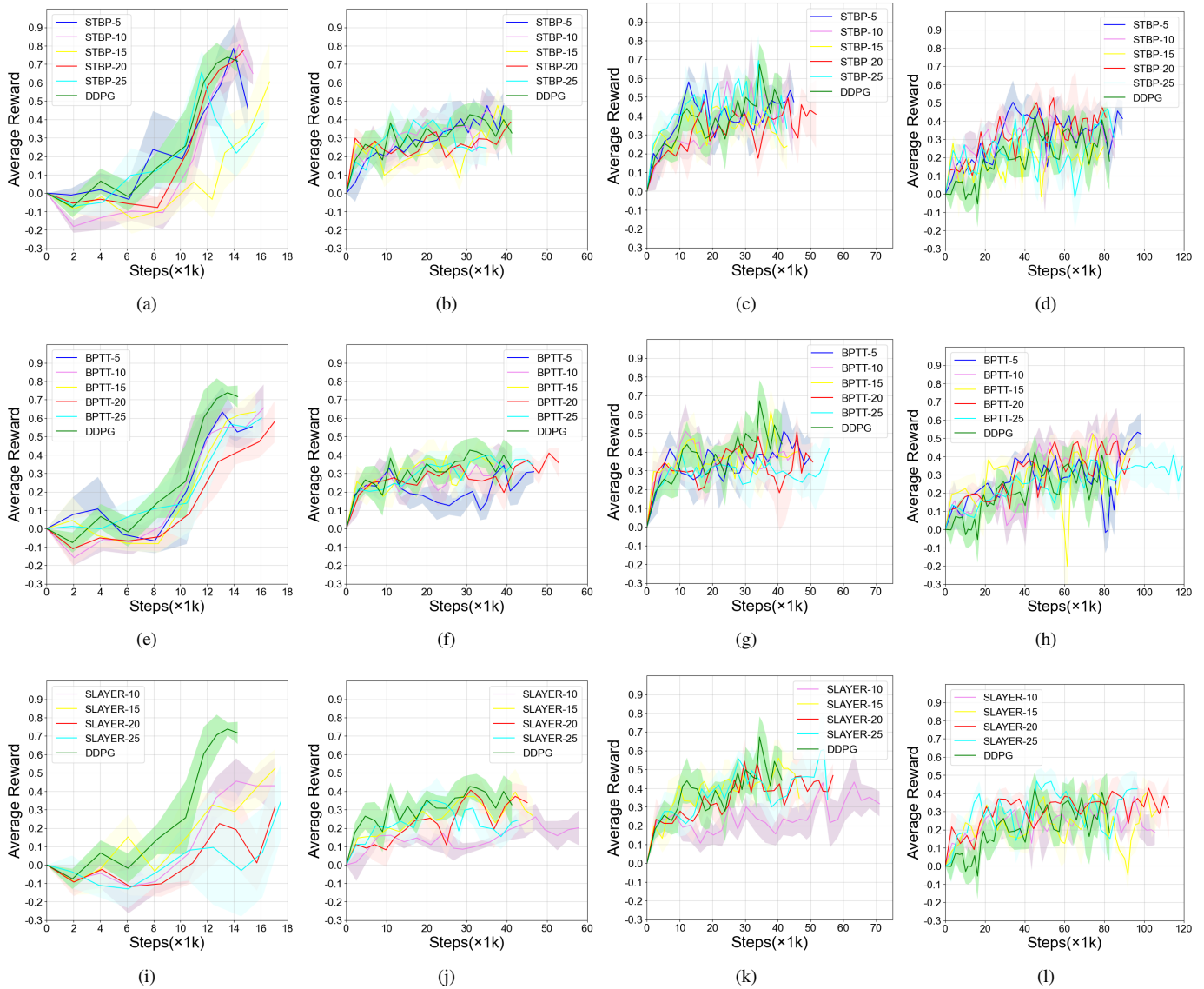


Fig. 8. Average reward curves of hybrid actor-critic network of our proposed HDDDPG (with various SNN training frameworks and different time steps) and original DDPG. (a) HDDDPG-STBP, training environment #1. (b) HDDDPG-STBP, training environment #2. (c) HDDDPG-STBP, training environment #3. (d) HDDDPG-STBP, training environment #4. (e) HDDDPG-BPTT, training environment #1. (f) HDDDPG-BPTT, training environment #2. (g) HDDDPG-BPTT, training environment #3. (h) HDDDPG-BPTT, training environment #4. (i) HDDDPG-SLAYER, training environment #1. (j) HDDDPG-SLAYER, training environment #2. (k) HDDDPG-SLAYER, training environment #3. (l) HDDDPG-SLAYER, training environment #4.

7700 and the GPU is Nvidia GTX 1650.

### B. Performance Analysis in Training

Here, we compare the training performance of HDDDPG based on three SNN training frameworks including STBP, BPTT and SLAYER and original DDPG. We analyze average reward and training time respectively.

1) *Average Reward*: We plot the average reward curves of HDDDPG based on the three SNN training frameworks with different time steps and original DDPG in the four training environments respectively, as shown in Fig. 8. The average reward is calculated by averaging all rewards in a period. Specifically, the average reward of HDDDPG-STBP in training environment #1/#2/#3 is similar to that of original DDPG,

but in training environment #4, HDDDPG-STBP can achieve higher average reward than original DDPG at the beginning, which means that HDDDPG-STBP learns the appropriate navigation policy quickly. The average reward of HDDDPG-BPTT is slightly worse than that of original DDPG in training environment #1/#2, and similar in training environment #3. In training environment #4, HDDDPG-BPTT also learns an appropriate navigation policy faster than original DDPG and finally achieves similar average reward. HDDDPG-SLAYER performs significantly worse than original DDPG in training environments #1/#2/#3, especially when the time step  $T$  is 10. But in training environment #4, HDDDPG-SLAYER can also learn the appropriate navigation policy faster, and finally achieve similar average reward to original DDPG. The above situation shows that in the face of a complex environment,

the spatio-temporal dynamic characteristics of SNN can better help the actor network learn a suitable navigation policy. In conclusion the average reward of HDDPG-STBP is close to that of original DDPG and is higher to HDDPG-BPTT and HDDPG-SLAYER.

2) *Training Time*: In this experiment, we compare the training time of HDDPG based on the three SNN training frameworks with different steps and original DDPG. The experimental results are shown in Fig. 9. With the increase of the time step, the training time of HDDPG based on the three SNN training frameworks shows different trends. The total training time of DDPG is the shortest, and the total training time of HDDPG-STBP is the closest to original DDPG. The total training time of HDDPG-STBP decreases with the decrease of the time step, which finally is close to that of original DDPG. For both STBP and BPTT training frameworks, since they use an iterative form similar to recurrent networks in the time dimension, the training time increases with larger time step. Here HDDPG-BPTT is implemented by the Sinabs framework<sup>4</sup>, and the training time increases significantly with the time step. In contrast, the training time of HDDPG-STBP increases less with the time step increasing than that of HDDPG-BPTT. For the SLAYER training framework, as the time step increases, the total training time remains close. This is because the SLAYER framework uses 3D convolution operations to achieve propagation in the time dimension, so the training time of HDDPG-SLAYER is not sensitive to the increase of the time step.

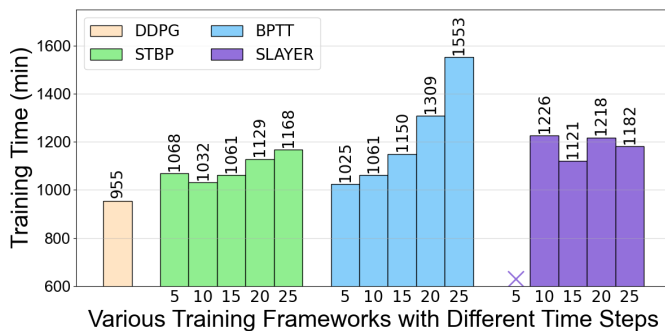


Fig. 9. Total training time of our proposed HDDPG (with various SNN training frameworks and different time steps) and original DDPG.

### C. Performance Analysis in Evaluation

In this subsection, we evaluate the navigation success rate, average distance, and average speed of HDDPG based on three SNN training frameworks with different steps and original DDPG in two evaluation environments, and a comprehensive analysis is carried out. In evaluation environment #1, the maximum allowable height of the MAV is set to 3.1m. In order to adapt to the expansion of the environment, the maximum allowable height of the MAV in the evaluation environment #2 is set to 3.6m.

<sup>4</sup>Sinabs Website: <https://pypi.org/project/sinabs>.

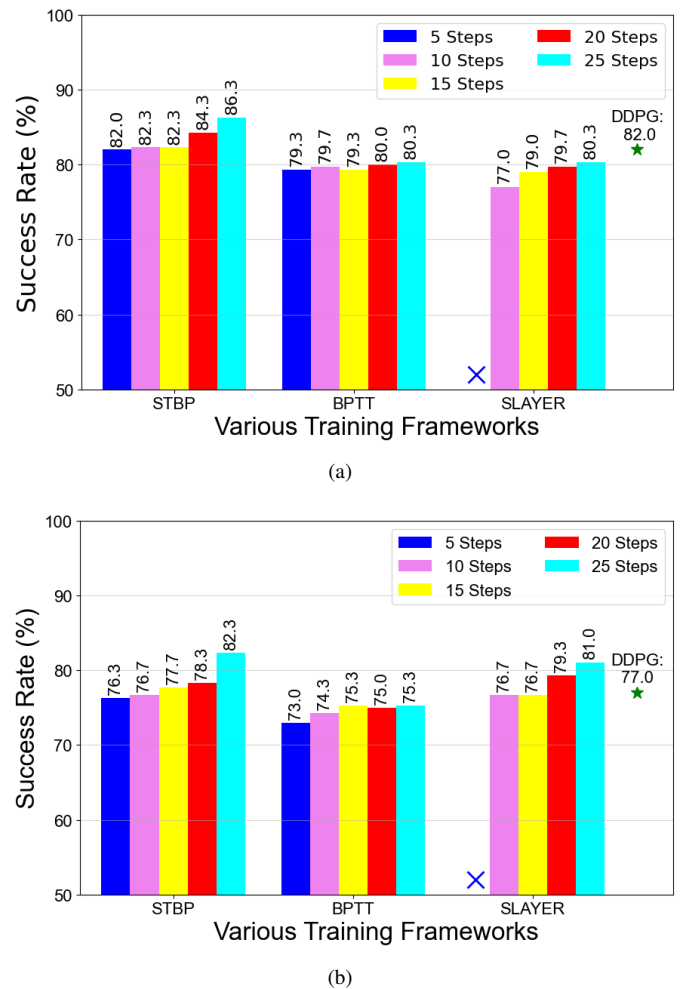


Fig. 10. Success rates in evaluation environments of our proposed HDDPG (with various SNN training frameworks and different time steps) and original DDPG. (a) Evaluation environment #1. (b) Evaluation environment #2.

1) *Success Rate*: For the HDDPG algorithm, we select the time steps  $T = 5, 10, 15, 20, 25$  respectively. The experimental results are shown in Fig. 10. In order to exclude chance, we repeat the experiment three times for each method and take the average value. The results show that the success rate of HDDPG-STBP, HDDPG-BPTT and HDDPG-SLAYER show a slight increase with the increase of time step in both evaluation environment #1 and evaluation environment #2. This is due to higher time step can bring higher control accuracy. In evaluation environment #1 (as shown in Fig. 10(a)), the success rate of DDPG is 82.0%. Taking this as a benchmark, the success rate of HDDPG-STBP can be significantly higher than that of original DDPG when the time steps are  $T = 10, 15, 20, 25$ , with a maximum increase of about 4.3%. Both HDDPG-BPTT and HDDPG-SLAYER are overall slightly lower than the original DDPG benchmark. In evaluation environment #2, the success rate of original DDPG is 77.0%. Since evaluation environment #2 is relatively more complex, original DDPG drops by about 5.0% compared to evaluation environment #1 (as shown in Fig. 10(b)). Taking this as a benchmark, the success rate of HDDPG-STBP can

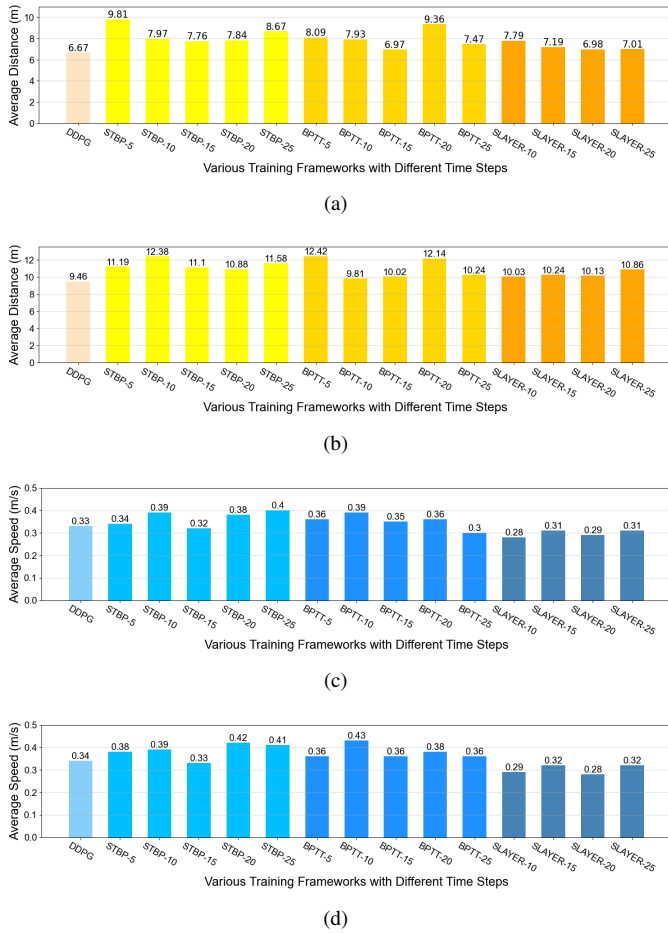


Fig. 11. Average distance and average velocity of HDDPG and DDPG by various training frameworks with different time steps. (a) Average distance in evaluation environment #1. (b) Average distance in evaluation environment #2. (c) Average speed in evaluation environment #1. (d) Average speed in evaluation environment #2.

be significantly higher than that of original DDPG when the time steps are  $T = 15, 20, 25$ , with a maximum improvement of about 5.3%. The success rate of HDDPG-SLAYER is slightly higher than that of original DDPG at the time steps  $T = 20, 25$ , and the highest improvement is about 4.0%. HDDPG-BPTT is slightly lower than original DDPG as a whole.

2) *Average Distance and Average Speed:* The average distance and average speed in evaluation environment #1 are shown in Fig. 11(a) and 11(b). In terms of average distance, the average distance of the path generated by original DDPG is the shortest. The average distance of HDDPG-STBP and HDDPG-BPTT is higher than that of original DDPG, thus the model obtained based on these two frameworks will cause the MAV to fly slightly upward compared with the model obtained by original DDPG. But these two frameworks can have faster average speed. These two frameworks trade off a portion of the distance for faster flight speed. The flying height of HDDPG-SLAYER is basically the same as that of original DDPG, so the average distance of HDDPG-SLAYER is the smallest among the three SNN training frameworks, but the average speed is also the lowest. The average distance and average speed in

evaluation environment #2 are shown in Fig. 11(c) and 11(d). As the evaluation environment expanded, the average distance for each method increased. In evaluation environment #2, the average distance and average speed showed the same regularity as in evaluation environment #1.

#### D. Flight Trajectory Analysis in Evaluation

In this section, we show and analyze the navigation trajectories (both successful and failed trajectories) of each method in two evaluation environments.

In Fig. 12, we show the success and failure trajectories of the four methods in evaluation environment #1. In Fig. 12(a)-12(d) of the successful trajectories, the highest heights of most trajectories of original DDPG are concentrated between 1.5m-2m, and the highest heights of individual trajectories reach between 2m-2.5m. Most of the trajectories of HDDPG-STBP have the highest heights between 2m and 2.5m, and two trajectories have the highest heights between 2.5m and 3m. The maximum heights of the trajectories of HDDPG-BPTT are concentrated between 2m and 3m. The trajectories of HDDPG-SLAYER are similar to that of original DDPG. In evaluation environment #1, the trajectories of original DDPG and HDDPG-SLAYER are the most stable, the average maximum height of the trajectories of HDDPG-STBP are slightly higher, and the average maximum height of the trajectories of HDDPG-BPTT are the highest. In the failure trajectories in Fig. 12(e)-12(h), the reasons for the failure of each method's trajectories due to collisions are similar: (1) The visual sensor carried by the MAV is depth camera. Compared with lidar, the field of view of the depth camera is smaller and only forward-looking, so it is easy to turn and collide without perceiving the obstacle; (2) the global geometric information is lacking, so that the trajectory is close to the obstacle sometimes. So the MAV lack enough space to avoid obstacles.

In Fig. 13, we show the success and failure trajectories of the four methods in evaluation environment #2. Due to the enlargement of the whole environment, each method has the situation that the maximum height of the trajectories rise. In Fig. 13(a)-13(d) of the successful trajectories, the highest heights of most trajectories of original DDPG and HDDPG-SLAYER are concentrated between 2m-2.5m, and the highest heights of individual trajectories will reach between 2.5m-3m, The highest heights of the trajectories of HDDPG-STBP and HDDPG-BPTT are concentrated between 2.5m-3m, and there are very few trajectories with the highest heights appearing between 3m-3.5m. In evaluation environment #2, the trajectories of original DDPG and HDDPG-SLAYER are the most stable, and the average maximum heights of the trajectories of HDDPG-STBP and HDDPG-BPTT is slightly higher. In the failure trajectories Fig. 13(e)-13(h), besides the reasons mentioned above, there is another reason that the increase in size and number of obstacles in evaluation environment #2 makes the MAV face more complex situations than the training environment. Faced with individual states, it is difficult for the actor network to map to appropriate actions, resulting in collisions.

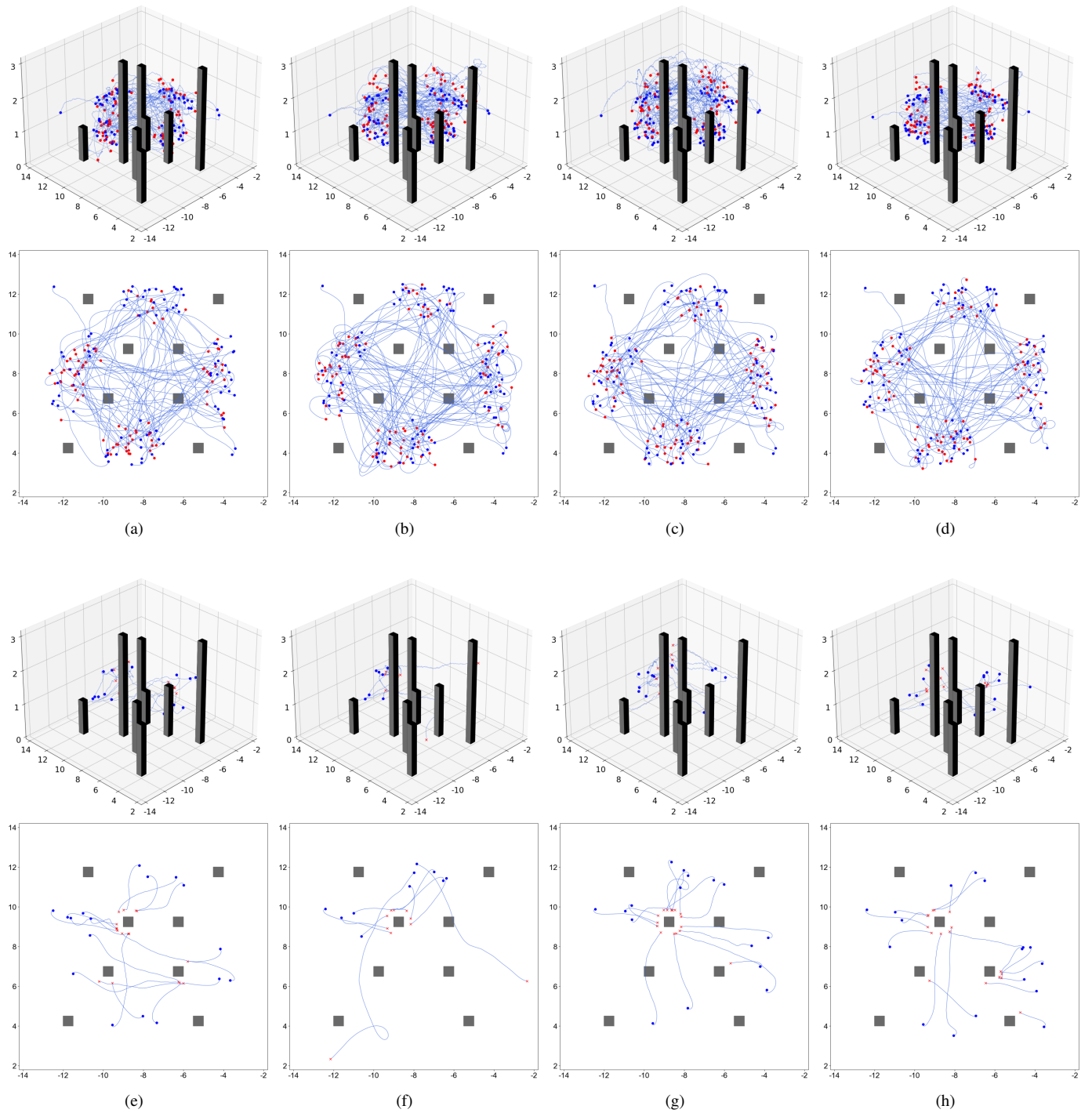


Fig. 12. Success and failure trajectories in evaluation environment #1. (a)-(d): Success trajectories over 200 random start and goal points of the four trained models obtained by original DDPG, HDDPG-STBP, HDDPG-BPTT and HDDPG-SLAYER (3D and top view). (e)-(h): Corresponding failure trajectories (3D and top view). (a) DDPG, success. (b) HDDPG-STBP, success. (c) HDDPG-BPTT, success. (d) HDDPG-SLAYER, success. (e) DDPG, failure. (f) HDDPG-STBP, failure. (g) HDDPG-BPTT, failure. (h) HDDPG-SLAYER, failure.

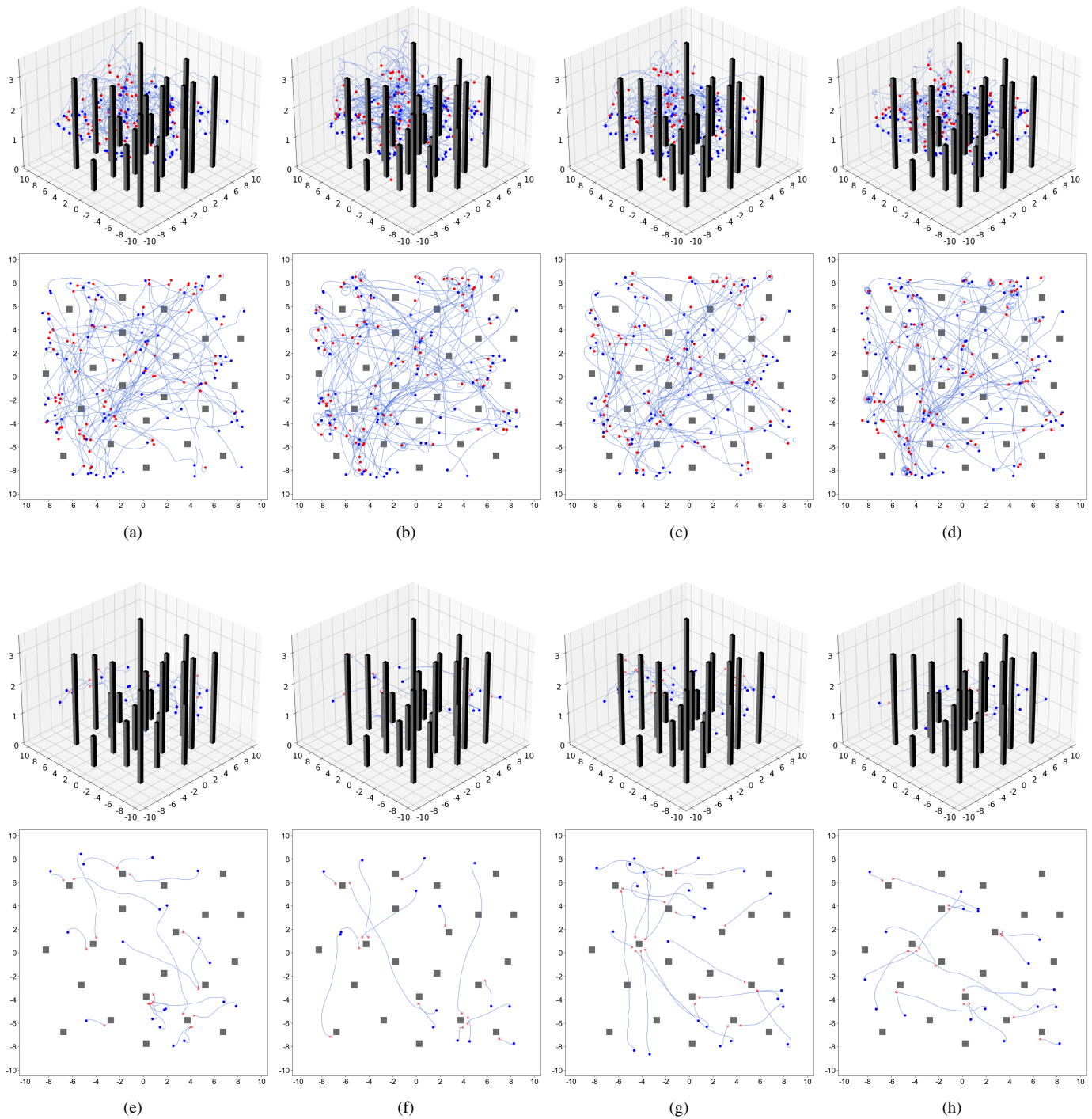


Fig. 13. Success and failure trajectories in evaluation environment #2. (a)-(d): Success trajectories over 200 random start and goal points of the four trained models obtained by original DDPG, HDDPG-STBP, HDDPG-BPTT and HDDPG-SLAYER (3D and top view). (e)-(h): Corresponding failure trajectories (3D and top view). (a) DDPG, success. (b) HDDPG-STBP, success. (c) HDDPG-BPTT, success. (d) HDDPG-SLAYER, success. (e) DDPG, failure. (f) HDDPG-STBP, failure. (g) HDDPG-BPTT, failure. (h) HDDPG-SLAYER, failure.

## V. CONCLUSIONS

In this paper, we propose a neuromorphic method combining deep reinforcement learning and spiking neural network, which is applied to the MAV 3D visual navigation for the first time and achieves comparable navigation performance. Our neuromorphic reinforcement learning framework adopts actor-critic network architecture. Combining with the deep critic network, we train the spiking actor network directly by STBP, BPTT and SLAYER three training frameworks respectively. Then, we evaluate the impact of different time steps of three training frameworks. The experimental results show that in two unfamiliar evaluation environments, the spiking actor network trained with the STBP framework can achieve a success rate better than that of the artificial neural network. The spiking actor network shows better robust trained with the SLAYER framework. Although our method can successfully achieve navigation in unfamiliar environments, but due to the lack of global geometric information that the map can provide in traditional navigation algorithms, it is difficult for MAV to achieve a global path that satisfies geometric constraints. In the future, we will consider adding geometric information to the reward function to achieve a better flight path and using a lower-level control method to enable the MAV to achieve higher-speed navigation. Furthermore, we will try to combine neuromorphic vision sensors (such as event cameras [36] [37] [38]) to enable neuromorphic 3D visual navigation of MAV.

## REFERENCES

- [1] Y. Lu, Z. Xue, G.-S. Xia, and L. Zhang, "A survey on vision-based uav navigation," *Geo-spatial information science*, vol. 21, no. 1, pp. 21–32, 2018.
- [2] S. Ross, N. Melik-Barkhudarov, K. S. Shankar, A. Wendel, D. Dey, J. A. Bagnell, and M. Hebert, "Learning monocular reactive uav control in cluttered natural environments," in *2013 IEEE international conference on robotics and automation*. IEEE, 2013, pp. 1765–1772.
- [3] Z. Fang, S. Yang, S. Jain, G. Dubey, S. Roth, S. Maeta, S. Nuske, Y. Zhang, and S. Scherer, "Robust autonomous flight in constrained and visually degraded shipboard environments," *Journal of Field Robotics*, vol. 34, no. 1, pp. 25–52, 2017.
- [4] Y. Lin, F. Gao, T. Qin, W. Gao, T. Liu, W. Wu, Z. Yang, and S. Shen, "Autonomous aerial navigation using monocular visual-inertial fusion," *Journal of Field Robotics*, vol. 35, no. 1, pp. 23–51, 2018.
- [5] K. Mohta, M. Watterson, Y. Mulgaonkar, S. Liu, C. Qu, A. Makeneni, K. Saulnier, K. Sun, A. Zhu, J. Delmerico *et al.*, "Fast, autonomous flight in gps-denied and cluttered environments," *Journal of Field Robotics*, vol. 35, no. 1, pp. 101–120, 2018.
- [6] H. Oleynikova, Z. Taylor, A. Millane, R. Siegwart, and J. Nieto, "A complete system for vision-based micro-aerial vehicle mapping, planning, and flight in cluttered environments," *arXiv preprint arXiv:1812.03892*, 2018.
- [7] F. Gao, W. Wu, W. Gao, and S. Shen, "Flying on point clouds: Online trajectory generation and autonomous navigation for quadrotors in cluttered environments," *Journal of Field Robotics*, vol. 36, no. 4, pp. 710–733, 2019.
- [8] X. Zhou, Z. Wang, H. Ye, C. Xu, and F. Gao, "Ego-planner: An esdf-free gradient-based local planner for quadrotors," *IEEE Robotics and Automation Letters*, vol. 6, no. 2, pp. 478–485, 2020.
- [9] X. Zhou, X. Wen, Z. Wang, Y. Gao, H. Li, Q. Wang, T. Yang, H. Lu, Y. Cao, C. Xu *et al.*, "Swarm of micro flying robots in the wild," *Science Robotics*, vol. 7, no. 66, p. eabm5954, 2022.
- [10] D. Silver, S. Singh, D. Precup, and R. S. Sutton, "Reward is enough," *Artificial Intelligence*, vol. 299, p. 103535, 2021.
- [11] K. Roy, A. Jaiswal, and P. Panda, "Towards spike-based machine intelligence with neuromorphic computing," *Nature*, vol. 575, no. 7784, pp. 607–617, 2019.
- [12] V. Mnih, K. Kavukcuoglu, D. Silver, A. A. Rusu, J. Veness, M. G. Bellemare, A. Graves, M. Riedmiller, A. K. Fidjeland, G. Ostrovski *et al.*, "Human-level control through deep reinforcement learning," *nature*, vol. 518, no. 7540, pp. 529–533, 2015.
- [13] T. P. Lillicrap, J. J. Hunt, A. Pritzel, N. Heess, T. Erez, Y. Tassa, D. Silver, and D. Wierstra, "Continuous control with deep reinforcement learning," *arXiv preprint arXiv:1509.02971*, 2015.
- [14] L. Tai and M. Liu, "A robot exploration strategy based on q-learning network," in *2016 IEEE international conference on real-time computing and robotics (rcar)*. IEEE, 2016, pp. 57–62.
- [15] L. Xie, S. Wang, A. Markham, and N. Trigoni, "Towards monocular vision based obstacle avoidance through deep reinforcement learning," *arXiv preprint arXiv:1706.09829*, 2017.
- [16] L. Tai, G. Paolo, and M. Liu, "Virtual-to-real deep reinforcement learning: Continuous control of mobile robots for mapless navigation," in *2017 IEEE/RSJ International Conference on Intelligent Robots and Systems (IROS)*. IEEE, 2017, pp. 31–36.
- [17] P. Mirowski, R. Pascanu, F. Viola, H. Soyer, A. J. Ballard, A. Banino, M. Denil, R. Goroshin, L. Sifre, K. Kavukcuoglu *et al.*, "Learning to navigate in complex environments," *arXiv preprint arXiv:1611.03673*, 2016.
- [18] V. Mnih, A. P. Badia, M. Mirza, A. Graves, T. Lillicrap, T. Harley, D. Silver, and K. Kavukcuoglu, "Asynchronous methods for deep reinforcement learning," in *International conference on machine learning*. PMLR, 2016, pp. 1928–1937.
- [19] Y. Zhu, R. Mottaghi, E. Kolve, J. J. Lim, A. Gupta, L. Fei-Fei, and A. Farhadi, "Target-driven visual navigation in indoor scenes using deep reinforcement learning," in *2017 IEEE international conference on robotics and automation (ICRA)*. IEEE, 2017, pp. 3357–3364.
- [20] R. B. Grando, J. C. de Jesus, and P. L. Drews-Jr, "Deep reinforcement learning for mapless navigation of unmanned aerial vehicles," in *2020 Latin American Robotics Symposium (LARS), 2020 Brazilian Symposium on Robotics (SBR) and 2020 Workshop on Robotics in Education (WRE)*. IEEE, 2020, pp. 1–6.
- [21] T. Haarnoja, A. Zhou, K. Hartikainen, G. Tucker, S. Ha, J. Tan, V. Kumar, H. Zhu, A. Gupta, P. Abbeel *et al.*, "Soft actor-critic algorithms and applications," *arXiv preprint arXiv:1812.05905*, 2018.
- [22] R. B. Grando, J. C. de Jesus, V. A. Kich, A. H. Kolling, and P. L. J. Drews-Jr, "Double critic deep reinforcement learning for mapless 3d navigation of unmanned aerial vehicles," *Journal of Intelligent & Robotic Systems*, vol. 104, no. 2, pp. 1–14, 2022.
- [23] C. Wang, J. Wang, Y. Shen, and X. Zhang, "Autonomous navigation of uavs in large-scale complex environments: A deep reinforcement learning approach," *IEEE Transactions on Vehicular Technology*, vol. 68, no. 3, pp. 2124–2136, 2019.
- [24] C. Wang, J. Wang, J. Wang, and X. Zhang, "Deep-reinforcement-learning-based autonomous uav navigation with sparse rewards," *IEEE Internet of Things Journal*, vol. 7, no. 7, pp. 6180–6190, 2020.
- [25] L. He, A. Nabil, and B. Song, "Explainable deep reinforcement learning for uav autonomous navigation," *arXiv preprint arXiv:2009.14551*, 2020.
- [26] M. H. Lee and J. Moon, "Deep reinforcement learning-based uav navigation and control: A soft actor-critic with hindsight experience replay approach," *arXiv preprint arXiv:2106.01016*, 2021.
- [27] M. Andrychowicz, F. Wolski, A. Ray, J. Schneider, R. Fong, P. Welinder, B. McGrew, J. Tobin, O. Pieter Abbeel, and W. Zaremba, "Hindsight experience replay," *Advances in neural information processing systems*, vol. 30, 2017.
- [28] W. Maass, "Networks of spiking neurons: the third generation of neural network models," *Neural networks*, vol. 10, no. 9, pp. 1659–1671, 1997.
- [29] Y. Wu, L. Deng, G. Li, J. Zhu, and L. Shi, "Spatio-temporal backpropagation for training high-performance spiking neural networks," *Frontiers in neuroscience*, vol. 12, p. 331, 2018.
- [30] P. J. Werbos, "Backpropagation through time: what it does and how to do it," *Proceedings of the IEEE*, vol. 78, no. 10, pp. 1550–1560, 1990.
- [31] S. B. Shrestha and G. Orchard, "Slayer: Spike layer error reassignment in time," *Advances in neural information processing systems*, vol. 31, 2018.
- [32] L. Meier, D. Honegger, and M. Pollefeys, "Px4: A node-based multithreaded open source robotics framework for deeply embedded platforms," in *2015 IEEE international conference on robotics and automation (ICRA)*. IEEE, 2015, pp. 6235–6240.
- [33] Y. Bengio, J. Louradour, R. Collobert, and J. Weston, "Curriculum learning," in *Proceedings of the 26th annual international conference on machine learning*, 2009, pp. 41–48.
- [34] A. Graves, M. G. Bellemare, J. Menick, R. Munos, and K. Kavukcuoglu, "Automated curriculum learning for neural networks," in *international conference on machine learning*. PMLR, 2017, pp. 1311–1320.

- [35] P. Soviany, R. T. Ionescu, P. Rota, and N. Sebe, “Curriculum learning: A survey,” *arXiv preprint arXiv:2101.10382*, 2021.
- [36] G. Gallego, T. Delbrück, G. Orchard, C. Bartolozzi, B. Taba, A. Censi, S. Leutenegger, A. J. Davison, J. Conradt, K. Daniilidis *et al.*, “Event-based vision: A survey,” *IEEE transactions on pattern analysis and machine intelligence*, vol. 44, no. 1, pp. 154–180, 2020.
- [37] D. Kong, Z. Fang, K. Hou, H. Li, J. Jiang, S. Coleman, and D. Kerr, “Event-vpr: End-to-end weakly supervised deep network architecture for visual place recognition using event-based vision sensor,” *IEEE Transactions on Instrumentation and Measurement*, 2022.
- [38] T.-H. Wu, C. Gong, D. Kong, S. Xu, and Q. Liu, “A novel visual object detection and distance estimation method for hdr scenes based on event camera,” in *2021 7th International Conference on Computer and Communications (ICCC)*. IEEE, 2021, pp. 636–640.



**Hao Zhuang** received the B.S. degree in robot engineering from Northeastern University, China, in 2021. He is currently pursuing the M.S. degree in robot science and engineering with Northeastern University, China. His research interests include event-based vision, visual-inertial odometry, and deep learning.



**Junjie Jiang** received the B.S. degree in automation from Northeastern University at Qinhuangdao, China, in 2020. He is currently pursuing the M.S. degree in robot science and engineering with Northeastern University, China. His research interests include spiking neural network, robot visual navigation, and reinforcement learning.



**Delei Kong** received the B.S. degree in automation from Henan Polytechnic University, China, in 2018, and the M.S. degree in control engineering from Northeastern University, China, in 2021. Since 2021, he has been a research assistant with Northeastern University, China. His research interests include event-based vision, robot visual navigation, and neuromorphic computing.



**Zheng Fang** (Member, IEEE) received the B.S. degree in automation and the Ph.D. degree in pattern recognition and intelligent systems from Northeastern University, China, in 2002 and 2006, respectively. He was a Postdoctoral Research Fellow of Carnegie Mellon University from 2013 to 2015. He is currently a Professor with the Faculty of Robot Science and Engineering, Northeastern University. His research interests include visual/laser SLAM, and perception and autonomous navigation of various mobile robots. He has published over 60 papers

in well-known journals or conferences in robotics and computer vision, including JFR, TPAMI, ICRA, IROS, BMVC, etc.



**Kuanxu Hou** received the B.S. degree in robot engineering from Northeastern University, China, in 2020. He is currently pursuing the M.S. degree in robot science and engineering with Northeastern University, China. His research interests include event-based vision, visual place recognition, and deep learning.



**Xinjie Huang** received the B.S. degree in robot engineering from Northeastern University, China, in 2021. He is currently pursuing the M.S. degree in robot science and engineering with Northeastern University, China. His research interests include event-based vision, visual SLAM, and deep learning.